Design and Control of a Dual-Stage Disk Drive Servo System with a High-Aspect Ratio Electrostatic Microactuator

Kenn Oldham, Sarah Felix, Richard Conway, and Roberto Horowitz

Computer Mechanics Laboratory

Mechanical Engineering

University of California, Berkeley, CA, USA

December 6, 2007

Abstract

Dual-stage servo systems have been proposed as a method for attaining increased bit densities from computer hard disk drives. To aid in controller operation, the second-stage microactuator used in a dual-stage system should operate at low voltages, feature relative position sensing, and have dynamics that interact well with those of the drive's original servo dynamics. This paper describes a high-aspect ratio electrostatic microactuator modified to improve dynamic interactions, relative position sensor performance, and device yield. A multi-rate, multivariable control design technique was used to evaluate the closed-loop performance of a disk drive system with a microactuator and relative position sensing. Closed-loop simulations reveal that the proposed configuration can reduce off-track position error. Addressing both hardware design and control design, this paper demonstrates the success of an integrated mechatronic approach to hard disk drive servo control.

Introduction

The continual increase of bit densities in computer disk drives requires ever-improving performance from the mechanical systems within the drives. The data storage industry is currently targeting disk drive bit densities of 1 terabyte per square inch (Tbpsi). This will require read-write head positioning with 3σ tracking errors of less than 5 nm. A typical disk drive is shown in Fig. 1. As the disk spins, it causes turbulent airflow to move past the servo arm, exciting the resonant vibrations of the E-block and flexible suspension that support the read-write head over the disk. At 1 Tbpsi tracking errors, this high frequency airflow-induced vibration is expected to become the dominant obstacle to accurate servo system tracking.

A potential solution to airflow-induced vibration of the servo arm is to install a second actuator at the tip of the servo arm. Such a microactuator can have a higher bandwidth than the conventional voice-coil motor (VCM) in the disk drive, and can be located beyond the region of suspension vibration. Various disk drive dual-stage servo configurations place a microactuator in the flexible suspension [1] [2] [3] [4], between the suspension and slider containing the read-write head [5] [6] [7] [8], or inside the slider itself [9] [10]. These arrangements provide increasing bandwidth from the microactuator in exchange for increasing design and processing complexity. Microactuators described in the literature typically suffer from excessive voltage requirements and undesirable interactions between the dynamics of the actuator and of the servo arm when the actuator is installed. Previously reported designs have also tended to focus exclusively on actuation performance, neglecting other capabilities useful in a dual-stage system, such as relative-position sensing and high-conductivity interconnects.

The microactuator described in this paper incorporates many useful features that improve dual-stage servo performance. Deep-trench isolation and deep-reactive ion etching are used to provide high-force, low-voltage actuation, as described in previous articles. A novel flexure configuration allows in-plane and

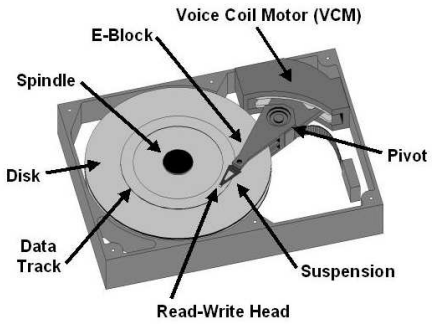

Figure 1: Mechanical components of a typical hard disk drive

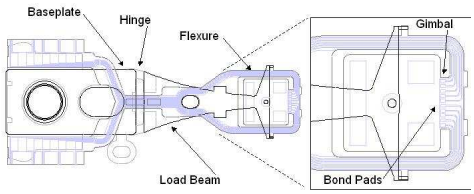

Figure 2: 15 mm MEMS-ready suspension

out-of-plane stiffness to be tailored individually to balance requirements on microactuator dynamics during read-write head flight. The microactuator includes dedicated capacitive sensing arrays for high-resolution relative position sensing, and the microactuator fabrication process has been revised to greatly improve interconnect quality and sensor performance. Completed microactuators have been successfully installed on multi-piece suspensions (Fig. 2) with improved vibration behavior over previous models, permitting more aggressive dual-stage controller designs.

Finally, complete system models were obtained based on experimental responses of the microactuator and capacitive sensor. The models were used to design a multi-input-multi-output (MIMO), multi-rate controller. The controller synthesis incorporated several constraints that reflect physical limitations of the microactuator and relative position sensing limitations. Closed-loop simulations provided insight into how the device design affects closed-loop performance.

Microactuator Design

The high-aspect ratio microactuator consists of a central shuttle holding the slider and read-write head driven by gap-closing electrostatic parallel-plate fingers. A schematic view of the microactuator structure is shown in Fig. 3. Differential parallel-plate arrays are interlaced using deep-trench isolation. This feature along with high-aspect ratio trenches produced by deep reactive-ion etching (DRIE) result in excellent force generation, as has been described in previous publications [11] [12]. The differential configuration results in an actuation force that is linear to within 5% over a 1 μm stroke length. The linearized actuation force, F, is given by the equation

$$F = 2\epsilon V V_b \frac{tL_f}{g_0^2} N_f \tag{1}$$

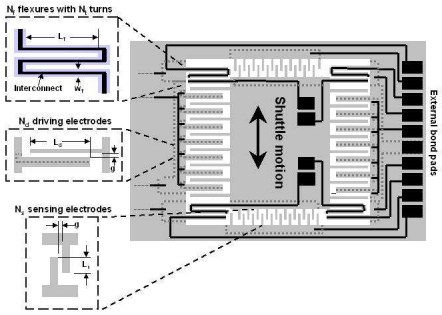

Figure 3: Schematic layout of a high-aspect ratio microactuator

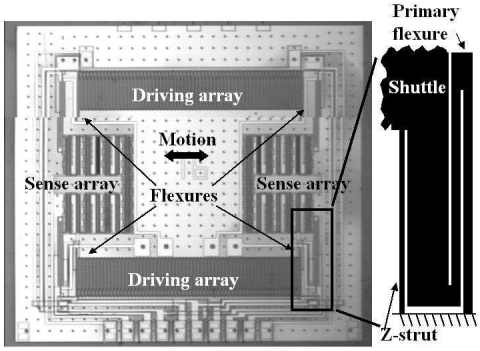

Figure 4: Full microactuator layout, with hybrid flexure design

where ϵ is the permittivity of air, V is the applied input voltage, V_b is a DC bias voltage on the shuttle fingers, t is the device thickness, L_f is the driving finger length, g_0 is the nominal gap between fingers, and N_f is the number of driving fingers.

Four pairs of flexures support the moving shuttle, with one pair located at each corner. The full layout of the device is shown in Fig. 4, with the flexure design expanded. Each flexure pair includes a long, wide main spring and a narrow z-strut. The main spring provides space for electrical interconnects and provides the bulk of resistance to in-plane motion, while the high-aspect ratio z-struts add significant out-of-plane stiffness with only a minor effect on in-plane motion. This allows the natural frequency of the microactuator to be precisely selected as best suited for closed-loop operation.

Sets of capacitive comb finger arrays act as position sensors to measure shuttle displacement relative to the tip of the disk drive suspension, known as the relative position error signal (RPES). The use of the RPES in dual-stage control can significantly improve closed-loop performance by permitting damping of microactuator resonant modes and preventing interference between VCM and microactuator motion [13]. The capacitive sensors are operated differentially, and the change in capacitance, ΔC_s, with displacement,

Table 1: Nominal microactuator design parameters and expected performance

Parameter (units)	Label	Value
Device thickness (μm)	t	100
Mass of shuttle and actuator (mg)	m_tot	2.2
Trench widths (μm)	g_0	4.0
Number of actuator fingers	N_f	126
Actuator finger length (μm)	L_f	282
Main spring width (μm)	w_k	16
Total spring constant (N/m)	k_tot	497
Natural frequency (Hz)	ω_n	2140
Bias Voltage (V)	V_b	15
Force/Volt (μN/V)	F/V	77
Displacement/Volt (nm/V)	x/V	81
Number of sensor fingers	N_s	304
Sensor finger length (μm)	L_s	40
Sensor capacitance (pF)	C_s	2.7

Δx is given simply by the formula:

$$\frac{\Delta C_s}{\Delta x} = \epsilon_0 \frac{t}{g_0} N_s \tag{2}$$

where N_s is the number of sensor fingers.

Key microactuator design parameters and anticipated properties are listed in Table 1.

Microactuator Fabrication

Figure 5 shows the process flow for microactuator fabrication. Microactuators are fabricated from silicon-on-insulator wafers with a 100 μm thick device layer. Wafers are coated with highly-doped polysilicon to increase conductivity of vias and sensor electrodes. Deep-trench isolation trenches are defined by lighography and etched by DRIE (Fig. 5a). For electrical insulation, the trenches are coated by a thin 0.25 μm silicon nitride film deposited by Low Pressure Chemical Vapor Deposition (LPCVD). The remainder of the trenches is refilled with undoped LPCVD polysilicon, with a thickness of approximately 3 μm (Fig. 5b). Effective refill and planarization of the deep isolation trenches is critical to device quality. While the polysilicon film is highly conformal and is largely reliable in refilling the high-aspect ratio trenches, a brief reactive ion-etch (RIE) is performed to etch the polysilicon film back to the nitride surface, with an overetch to expose shallow keyholes in the refilled trenches. A second, 1 μm polysilicon deposition refills these keyholes and leaves a thinner layer of excess polysilicon on the wafer surface. This allows more precise control of a second etch-back and planarization step by chemical mechanical polishing (CMP). After polishing, a final 0.2 μm LPCVD

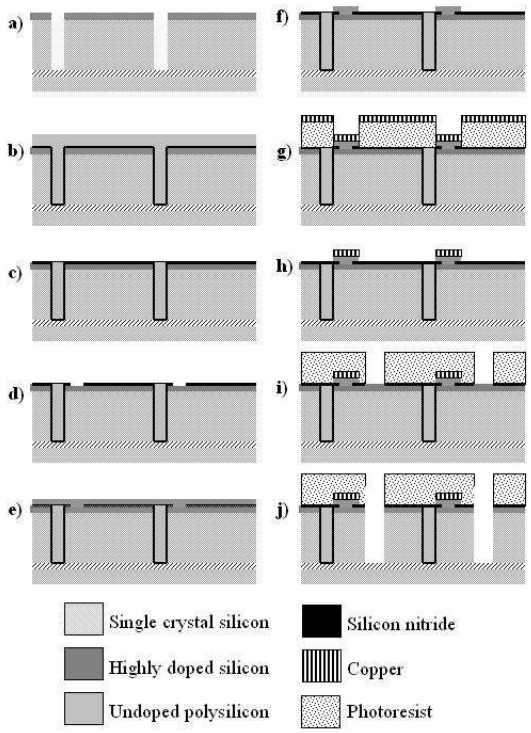

Figure 5: High-aspect ratio microactuator process flow

silicon nitride layer is deposited, completing the isolation trenches (Fig. 5c).

The CMP process provides an excellent surface for interconnect formation. Contact holes are patterned by lithography and etched through the silicon nitride film by RIE (Fig. 5d). Interconnects consist of a silicon-metal stack to provide mechanical robustness and high conductivity. A highly doped polysilicon film is deposited to provide a lower layer for the interconnects that is robust against damage during further wafer processing (Fig. 5e). The polysilicon film is patterned by lithography and etched by RIE (Fig. 5f). A chrome adhesion layer and 1000 $\AA$-thick copper film are then evaporated onto a 9 μm-thick, patterned, photoresist layer, to form the upper layer of the interconnects in a lift-off procedure (Fig. 5g,h). The copper layer provides improved conductivity and, due to its resistance to hydrofluoric acid, permits a dramatically simplified release procedure from previous microactuator fabrication processes.

A final lithography step and DRIE step are performed to define the electrostatic fingers and other features of the completed microactuator. During this final lithography step, a 9 μm-thick photoresist film is again necessary in order to encapsulate the metallized interconnects (Fig. 5i,k). The trench width targeted for this step was 4 μ, but erosion of trench sidewalls during the etching process resulted in actual trench widths as large as 8 μm. This proved to be a significant limitation on microactuator performance, as will be discussed

in Section V.

Microactuators are released from the wafer by breaking the tethers supporting the devices and immersing the dies in hydrofluoric acid (HF). Because copper is resistant to HF, this is a more efficient and higher yield release procedure than earlier releases using anisotropic etchants or backside plasma etching. The thick photoresist layer is dissolved in acetone, and microactuator fabrication is completed by cleaning the microactuator surface with O2 and SF6 plasmas.

Open-Loop Experimental Results

Finished microactuators were installed on 15 mm MEMS ready suspensions provided by Hutchinson Technology, Inc. Off-track vibration modes for these suspensions were expected to exceed 4 kHz in frequency, providing a wide separation from the natural frequency of the microactuator. This separation of modes improves dual-stage servo capabilities compared to microactuators installed on earlier, longer disk drive suspensions.

Microactuators were aligned to sliders and suspensions using bulk-micromachined silicon fixtures on a 3-DOF positioning stage. These fixtures were intended to reduce unwanted dynamics in the disk drive due to inaccuracies of the microactuator installation process. A slider is attached to a microactuator and the microactuator to a suspension using epoxy, after which ultrastonic wire bonding is used to create electrical connections between the suspension and microactuator. The assembled suspension assembly is then glued to a modified disk drive E-block with a slight bend at the tip to reduce slider pitch and metal strips attached to provide connections for electrical leads from the suspension. Finally, ultrasonic wire bonding is used to connect these metal strips and leads.

The assembled servo arm was installed in a commercial disk drive as shown in Fig. 6 with the disk removed. Displacement of the read-write head and suspension tip were measured using a Laser Doppler Velocimeter (LDV). A 2.5 cm disk was used to improve access and signal quality from the LDV. Rotation speed of the disk drive was 7200 rpm.

Fig. 7 shows the transfer function from microactuator input to read-write head displacement during disk drive operation. The microactuator has a natural frequency of 1780 Hz and a static gain of 17 μN/V. The natural frequency is located well away from suspension vibration modes occuring above 3.5 kHz. The actuation force meets or exceeds that of other published results for an actuated slider, despite trench erosion that widens that gaps betweens electrodes. The oversized trench width limits the performance of the actuator, as shown in Table 2, but the experimental gains are still adequate for vibration control.

Fig. 8 shows the transfer function from VCM input to displacement of the suspension tip and the read-

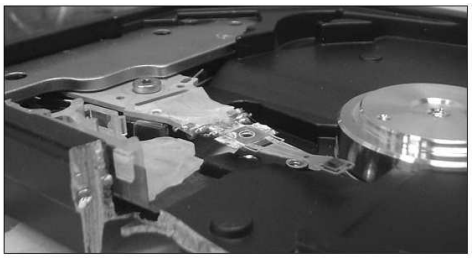

Figure 6: Assembled dual-stage test system

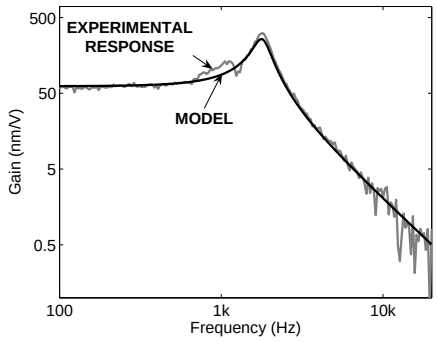

Figure 7: Experimental frequency response of high-aspect ratio microactuator during flight.

write head. The microactuator's resonant peak is visible between a low frequency vibration mode associated with the servo arm flex cable, and the higher frequency suspension vibration modes. It is clear that the microactuator dynamics attenuate head vibration even in open-loop, as the microactuator acts as a low pass filter between the suspension dynamics and read write head. However, the microactuator's own resonance may be excited by airflow, motivating the addition of relative position error sensing.

Relative position error sensing (RPES) was implemented using a fully differential capacitive sensing circuit with high-frequency modulation, as shown in the schematic in Fig. 9. The sensing circuit uses conventional

Table 2: Theoretical microactuator performance without and with trench erosion versus experimental results

	Theoretical performance, nominal trench width	Theoretical performance, actual trench width	Experimental performance
Gap width (μm)	4.0	7.6	7.6
Natural frequency (Hz)	2140	1600	1780
Static gain (μN/V)	77	18	17
Static gain (nm/V)	195	82	62
Damping ratio			12%

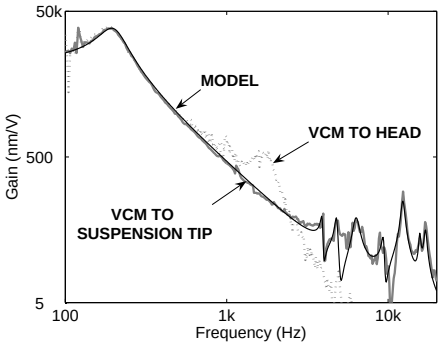

Figure 8: Experimental transfer functions from VCM input to read-write head (dashed) and suspension tip (gray line) displacement. Model of VCM to suspension tip transfer function is shown in black.

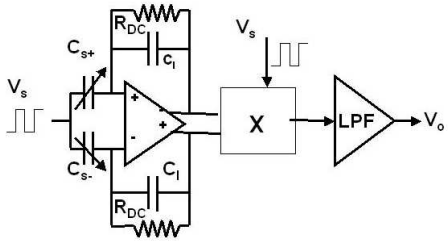

Figure 9: Schematic view of Relative Position Error Sensing circuit

high frequency multiplexing of the sensor input voltage to reduce noise and low frequency disturbance. A 3.3 V, 400 kHz square wave was used as the input voltage and modulation signal. The output low-pass filter was followed by a high-pass filter to form a pass band pass between 700 Hz and 4 kHz, in order to focus on the resonant peak of the microactuator, where disturbances to the microactuator motion result in the most significant errors in read-write head motion.

Fig. 10 shows the transfer function from microactuator input to sensor output during disk drive operation, along with a scaled view of the bandpass filter to show the underlying circuit dynamics. The resonant peak of the microactuator is plainly visible, even for relatively small microactuator motions. Sensor resolution is limited by high frequency disturbances and feedthrough distortions from the driving signal. The most significant high frequency "noise" source was ringing at the modulation frequency due to unmodeled mismatches in input resistance and parasitic capacitances between the two differential sensing capacitors. Feedthrough is the primary limitation on the resolution of capacitive sensing in many MEMS devices. While feedthrough in the proposed design is reduced by the low driving voltage of the microactuator and separate driving and sensing arrays, it is still a significant source of measurement error.

In tests of the microactuator alone, 3 nm sensor resolution in the presence of sensor noise and a worst

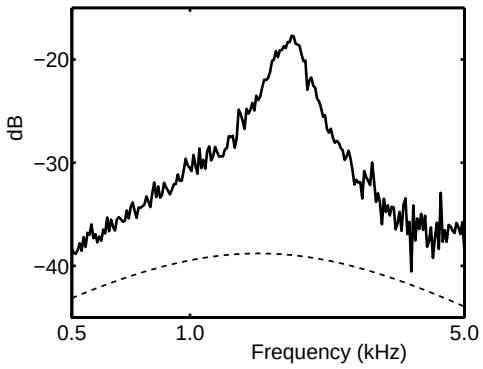

Figure 10: Transfer function from microactuator input to microactuator displacement (solid line), measured by the RPES circuit during flight, and the circuit's bandpass filter (dashed line), not to scale.

case feedthrough distortion of 6 nm were achieved. After installation, microactuator resolution is degraded to approximately 17 nm when measuring external "disturbances," such as motion excited by the VCM. Feedthrough and associated ringing due to microactuator input voltages cause even greater errors, with 40 nm resolution and 19 nm distortion due to feedthrough. The degradation in performance after installation is attributed to longer leads and larger parasitic capacitances when the suspension, E-block, and additional cables are placed between the microactuator and sensing circuitry. Ideally, sensing circuitry would be placed on the E-block itself to improve sensor performance. A more aggressive bandpass filter or controller-based model of feedthrough behavior could also potentially improve sensor resolution.

Closed-Loop Control Design and Simulation

To evaluate the benefit of microactuator improvements and relative position sensing for tracking control, a closed-loop controller was designed and simulated. The control design strategy is based on multi-rate multivariable control synthesis for dual stage hard disk drives described in [14]. The system is multi-rate since the capacitive sensing and actuators can operate at a higher rate than the fixed rate of the PES signal. In this paper, the sampling rate of the PES is 75 kHz, while the RPES sampling rate and the actuation rates are 150 kHz. [13] showed that this control scheme can achieve superior tracking performance compared to both single rate and single-input-single-output strategies.

The control design used in this study is different from that described in [14] in several ways. First, the control design considers H_2 control instead of mixed $H_2/H_{\inf}$. H_2 control is a more natural formulation for minimizing the variance of the PES. Second, the control synthesis is based on a nominal plant, ignoring robustness. This is useful for evaluating the performance of a given hardware configuration. Third, the constraints in the minimization are formulated differently. Here, explicit constraints are imposed on certain

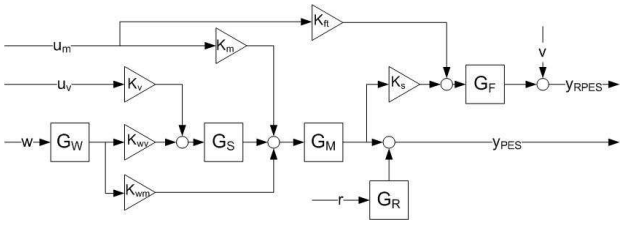

Figure 11: Block diagram of plant model.

signals such as control effort, while the PES is directly minimized. This is in contrast to minimizing a norm that reflects a combination of the PES along with other signals. As will be explained in the following, this turns out to be a useful tool for device design.

0.0.1 Plant Model

The complete system model for control design incorporates experimental results described in previous sections. Fig. 11 shows a block diagram of the plant model. The VCM and microactuator inputs are u_v and u_m, respectively. y_{PES} and y_{RPES} are the measurements corresponding to the subscripts. The remaining labels in the diagram will be described in the following.

The microactuator mode is modeled as a second order transfer function, with the natural frequency, ω_M, and damping ratio, ζ_M, estimated from the response shown in Fig. 7. The transfer function is

$$G_M(s) = \frac{1}{s^2 + \zeta_M \omega_M s + \omega_M^2}. \tag{3}$$

The model is shown in Fig. 7 along with the experimental results. Similarly, the suspension dynamics are modeled as a summation of N second order modes, with some modes neglected to keep model order manageable. The transfer function is given by

$$G_S(s) = \sum_{i=1}^{N} \frac{A_{si}}{s^2 + \zeta_{si}\omega_{si} s + \omega_{si}^2}, \tag{4}$$

where A_{si}, ζ_{si}, and ω_{si} are respectively the static gain, damping ratio and natural freqency of the ith mode. The model response is shown in Fig. 8. The suspension modes are excited by both the VCM and by windage. The gain vectors K_v, K_{wv}, capture the appropriate magnitude of these excitations, respectively. The microactuator dynamics are excited by suspension tip motion (the output of G_s), microactuator input, and windage. The gains K_m, K_{wm} correspond to the microactuator input and windage excitation, respectively.

The capacitive sensor is modeled with the following filter to reflect the circuit dynamics:

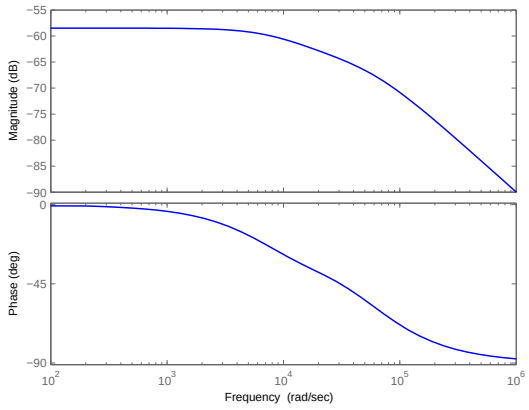

Figure 12: Bode diagram of G_w representing the frequency content of the windage disturbance.

Table 3: Model parameters.

Parameter (units)	Label	Value
Filter Gain	K_F	1.2
Low Pass Cutoff Frequency (Hz)	ω_L	4.2e3
High Pass Cutoff Frequency (Hz)	ω_H	2.3e4
Sensor Gain (V/nm)	K_S	5e5
Feedthrough Gain (V/V)	K_{ft}	18e-9*K_S
Sensor Noise Variance V^2	v	$(40e-9*K_S)^2$
Runout Noise Variance	r	1

$$G_F(s) = K_F^2 * (\frac{\omega_L}{s+\omega_L})^2 (\frac{\frac{1}{\omega_H}s}{\frac{1}{\omega_H}s+1})^2, \tag{5}$$

where K_F, ω_H, and ω_L are the filter gain, high pass cutoff frequency, and low pass cutoff frequency respectively. Sensor gain K_S represents the conversion of displacement to voltage. RPES sensor noise, represented by v in the block diagram, is white with a Gaussian distribution and a variance reflecting the 40nm resolution observed in the experimental results. In addition, feedthrough distortion is modeled by sending u_m through a gain, F_{ft} and adding this to the input to the sensor tranfer function, $G_F(s)$.

The system is subject to several exogenous input disturbances which are considered in H_2 control. Track runout, which consists of low frequency repeatable and non-repeatable disturbances, is modeled as white noise, r, filtered by a transfer function, $G_R(s)$. $G_R(s)$ was obtained from [13]. Windage is modeled as white noise, w, filtered by the transfer function $G_W(s)$, which was estimated from experimental data and is shown in Fig. 7. Table 3 summarizes values of various model parameters.

Table 4: Closed-loop control simulation results (3σ values).

Plant (Controller Order)	PES (nm)	RPES (nm)	u_v (V)	u_m (V)
Old plant, no RPES (11)	5.4	36.5	4.7	19.5
New plant, no RPES (15)	4.8	39.3	4.7	19.9
Maximum allowed		**1000**	**5**	**20**
New plant, with RPES (19)	5.6	38.5	4.5	4.9
Maximum allowed		**100**	**5**	**5**
New plant, with RPES (19)	4.8	27.8	4.3	16.0
Maximum allowed	**4.8**	**100**	**5**	

Control Design and Simulation

As mentioned above, the control synthesis incorporates constraints on certain quantities that can reflect hardware limitations. Specifically, the VCM input voltage, u_v, and microactuator voltage, u_m, as well as the RPES, are constrained. There were two considerations in setting the constraints: *physical limitations* and *sensing limitations*. The physical limitations of the input voltages are based on range of device operation and hardware experience. The physical limitation of the RPES is the displacement range of the capacitive arrays which avoids electrostatic pull-in. However, the previous section described limitations of the capacitive sensing circuit that reduce the range of meaningful measurements. Therefore, more strict constraints can also be imposed to ensure that this meaningful measurement range is not exceeded. Specifically, the actual RPES range can be narrowed, and u_m can be limited to avoid excessive feedthrough distortion.

For comparison, the control design was performed on the improved system with and without capacitive sensing, as well as an earlier model with older hardware [13] and no capacitive sensing. The target for tracking performance was 5 nm at 3σ.

First, controllers were designed for the old and new systems using physical constraints. With the multi-rate H_2 controller, the older design was able to achieve 5.4 nm tracking, which falls short of the target. However, the new system without capacitive sensing achieved 4.8 nm. This demonstrates that the hardware improvements alone were beneficial for tracking performance. Table 4 summarizes the 3σ values of the various signals along with their maximum allowed values. Note that both actuator voltages are near their respective constraint, indicating that both actuators are being used to their full capacity.

Next, capacitive sensing was introduced into the model with the new hardware. Constraints on RPES and u_m were tightened to reflect sensing limitations. As such, the closed-loop system was only able to achieve 5.6 nm. It is likely that tracking performance suffered due to imposing tighter limitations on the microactuator effort. To evaluate just how much microactuator effort would be needed along with capacitive sensing to

recover the 4.8 nm result, a final iteration was performed in which the PES signal is constrained to 4.8 nm and u_m is minimized. The resulting 3σ value of u_m (shown in Table 4) is lower than its physical constraint. This indicates that acceptable tracking is possible provided improvements can be made to the sensor measurement circuitry in the presence of higher microactuator driving voltages. Also note that improving microactuator gain with narrower trenches would allow more microactuator control at lower voltages, further alleviating the feedthrough limits on sensing. Finally, comparing the results of the second and fourth test, the effects of capacitive sensing appear to be lowering the microactuator voltage and reducing the RPES. This suggests that even better tracking performance could be achieved with capacitive sensing if u_m was allowed to reach its original limit. Note that along with improved tracking performance comes a higher controller order, summarized in Table 4, which is the results of greater complexity in the plant model.

Conclusions and Future Work

Conclusions

This paper presents an integrated mechatronic approach to hardware and control design for a hard disk drive servo system. It described several improvements to a previously-proposed dual-stage hard disk drive system using an electrostatic microactuator as the second stage input. Copper metallization of device interconnects improved conductivity as well as device yield and reliability. A new suspension geometry along with flexure design allowed the microactuator resonance to be separated from the higher-frequency suspension vibration modes, a desirable feature for control. An improved installation procedure contributed to more accurate and repeatable suspension dynamics. Finally, circuitry was developed to extract measurements from dedicated sensing arrays on the device, thus providing a relative position error signal.

Closed-loop simulations with a multi-rate, multivariable controller demonstrated that these hardware improvements were beneficial for tracking performance in a dual-stage hard disk drive. Further, the constrained H_2 control synthesis technique described proved to be a useful tool to evaluate hardware design with respect to closed-loop performance. It revealed that improvements to the capacitive sensing and microactuator trench width are critical for acceptable performance of the full system.

Future Work

Results show that feedthrough prevents RPES operation over a range that would improve overall system performance. This constraint could be eliminated by more sophisticated sensing circuitry along with higher microactuator gain. To improve sensing, the circuitry could be located on the E-block to reduce parasitic

capacitance. Better tuning of the modulation frequency could reduce ringing associated with unmodeled mismatches in circuit dynamics. A more aggressive band bass filter or a controller-based model of feedthrough behavior could further improve sensor resolution. In addition, the microactuator fabrication process should be revised to achieve more narrow trench widths in the actuation arrays. This would improve microactuator gain to achieve similar performance at lower voltages.

Bibliography

[1] R. Evans, J. Griesbach, and W. Messner, "Piezoelectric microactuator for dual-stage control," *IEEE Transactionson Magnetics*, vol. 35, pp. 977–81, Mar. 1999.

[2] M. Tokuyama, T. Shimizu, H. Masuda, S. Nakamura, M. Hanya, O. Iriuchijima, and J. Soga, "Development of ϕ-shaped actuated suspension for 100-ktpi hard disk drives," *IEEE Transactions on Magnetics*, vol. 33, no. 3, pp. 1184–6, Sept. 2001.

[3] I. Naniwa, S. Nakamura, S. Saegusa, and K. Sato, "Low voltage driven piggy-back actuator of hard disk drives," in *IEEE International MEMS 99 Conference*, Orlando, FL, USA, 1999, pp. 49–52.

[4] S. Koganezawa, K. Takaishi, Y. Mizoshita, Y. Uematsu, and T. Yamada, "Development of integrated piggyback milli-actuator for high density magnetic recording," in *International Conference on Micromechatronics for Information and Precision Equipment*, 1997, pp. 20–23.

[5] D. Horsley, *Ph.D. Dissertation: Microfabricated electrostatic actuators for magnetic disk drives.* Berkeley, CA, USA: University of California, 1998.

[6] T. Hirano, L. Fan, T. Semba, W. Lee, J. Hong, S. Pattanaik, P. Webb, W.-H. Juan, and S. Chan, "High-bandwidth hdd tracking servo by a moving-slider micro-actuator," *IEEE Transactions on Magnetics*, vol. 35, pp. 3670–72, september 1999.

[7] H. Fujita, K. Suzuki, M. Ataka, and S. Nakamura, "A microactuator for head positioning system of hard disk drives," *IEEE Transactionson Magnetics*, vol. 35, pp. 1006–10, March 1999.

[8] H. Kuwajima and K. Matsuoka, "Thin film piezoelectric dual-stage actuator for hdd," in *InterMag Europe, Session BS04*, Amsterdam, Netherlands, Apr. 2002, p. BS4.

[9] S. Nakamura, K. Suzuki, M. Ataka, and K. Mukasa, "An electrostatic microactuator for a magnetic head tracking system of hard disk drives," in *Advances in Information Storage Systems*, vol. 10, Singapore, Singapore, 1998, pp. 83–99.

[10] H. Toshiyoshi, M. Mita, and H. Fujita, "A mems piggyback actuator for hard-disk drives," *Journal of Microelectromechanical Systems*, vol. 11, no. 6, pp. 648–54, Dec. 2002.

[11] K. Oldham, X. Huang, and R. Horowitz, "Design, fabrication and control of a high-aspect ratio microactuator for vibration suppression in a hard disk drive," in *Proceedings of the 16th IFAC World Congress*, Prague, Czech Republic, 2005.

[12] T.-L. Chen, Y. Li, K. Oldham, and R. Horowitz, "Mems applications in computer disk drive dual-stage servo systems," *Journal of the Society of Instrument and Control Engineers*, vol. 41, no. 6, pp. 412–20, 2002.

[13] X. Huang, R. Nagamune, and R. Horowitz, "A comparison of multirate robust track-following control synthesis techniques for dual-stage and multi-sensing servo systems in hard disk drives," *IEEE Transactions on Magnetic Recording*, 2006.

[14] H. X. Nagamune, R. and R. Horowitz, "Multirate track-following control with robust stability for a dual-stage multi-sensing servo system in hdds," in *Proceedings of the 44th IEEE Conferenct on Decision and Control*, 2005, pp. 3886–91.